Supplemental Materials: Quantum Computation of Frequency-Domain Molecular Response Properties Using a Three-Qubit iToffoli Gate

Shi-Ning Sun,[1,*] Brian Marinelli,[2,3,*] Jin Ming Koh,[4] Yosep Kim,[5] Long B. Nguyen,[2,3] Larry Chen,[2,3] John Mark Kreikebaum,[2,6] David I. Santiago,[2,3] Irfan Siddiqi,[2,3,6] and Austin J. Minnich[1,†]

[1] *Division of Engineering and Applied Science, California Institute of Technology, Pasadena, CA 91125, USA*
[2] *Quantum Nanoelectronics Laboratory, Department of Physics, University of California at Berkeley, Berkeley, CA 94720, USA*
[3] *Computational Research Division, Lawrence Berkeley National Laboratory, Berkeley, California 94720, USA*
[4] *Division of Physics, Mathematics and Astronomy, California Institute of Technology, Pasadena, California 91125, USA*
[5] *Center for Quantum Information, Korea Institute of Science and Technology (KIST), Seoul 02792, Korea*
[6] *Materials Science Division, Lawrence Berkeley National Laboratory, Berkeley, California 94720, USA*

I. $\mathbb{Z}_2$ SYMMETRY TRANSFORMATIONS ON OPERATORS AND QUBIT STATES

In this section, we describe the $\mathbb{Z}_2$ symmetry transformations applied to the qubit operators and ancilla qubit subspaces in the linear combination of unitaries (LCU) algorithm. This transformation converts the four-qubit operators and qubit subspaces into two-qubit ones, which are used in constructing the circuits for hardware runs.

There are four spin orbitals in the diatomic molecules we study in this work. We order them as $0\uparrow, 0\downarrow, 1\uparrow, 1\downarrow$ from left to right, corresponding to the qubit indices 0, 1, 2, 3, in the Pauli strings and qubit state bitstrings. The HOMO-LUMO molecular Hamiltonians of NaH and KH have the same number of up-spin and down-spin electrons. After Jordan-Wigner transformation, the parity of up-spin and down-spin electrons correspond to the qubit operators $ZIZI$ and $IZIZ$, which are $\mathbb{Z}_2$ symmetries of the Hamiltonian. The mean-field ground state $|\Phi_0\rangle = |1100\rangle$ has the expectation values $\langle ZIZI\rangle = \langle IZIZ\rangle = -1$, as does the exact ground state $|\Psi_0\rangle$.

We can define three types of states in our calculation based on $\mathbb{Z}_2$ symmetries: the "up-spin" states are the states that have symmetries $\langle ZIZI\rangle = 1, \langle IZIZ\rangle = -1$, which are obtained by applying $\hat{a}_{p\uparrow}$ or $\hat{a}^\dagger_{p\uparrow}$ on the ground state; the "down-spin" states are the states that have symmetries $\langle ZIZI\rangle = -1, \langle IZIZ\rangle = 1$, which are obtained by applying $\hat{a}_{p\downarrow}$ or $\hat{a}^\dagger_{p\downarrow}$ on the ground state; the "spin-balanced" states are the states that have the symmetries $\langle ZIZI\rangle = -1, \langle IZIZ\rangle = -1$, which are obtained by applying the number operators on the ground state and have the same symmetries as the ground state. Note that the up-spin and down-spin states here are defined from the expectation values of the $\mathbb{Z}_2$ symmetry operators but not from the spin-z components of the corresponding molecular states. For example, the qubit computational state $|0100\rangle$ represents the molecular state with a single electron in the $0\downarrow$ orbital, which has total spin-z expectation value of $-1/2$, but in our definition it is classified as an up-spin state.

For each type of state, we aim to find a $\mathbb{Z}_2$ transformation that generates the minimum number of gates in the circuits that apply the creation or annihilation operators $\hat{a}^{(\dagger)}_{p\sigma}$ or the number operators $\hat{n}_{p\sigma}$. Recall from the main text that in the Jordan-Wigner transformation, the creation or annihilation operators $\hat{a}^{(\dagger)}_{p\sigma}$ have the decomposition $\bar{X}_{p\sigma} \pm i\bar{Y}_{p\sigma}$, where $\bar{X}_{p\sigma}$ and $\bar{Y}_{p\sigma}$ are the Jordan-Wigner transformed Pauli X and Y operators on orbital p with spin σ, and the number operators $\hat{n}_{p\sigma}$ have the decomposition $I - Z_{p\sigma}$. The transition amplitudes under the $\mathbb{Z}_2$ transformation $U_{\mathbb{Z}_2}$ can be expressed as

$$\langle\Psi^{N\pm1}_\lambda|\hat{a}^{(\dagger)}_{p\sigma}|\Psi_0\rangle = \langle\Psi^{N\pm1}_\lambda|U^\dagger_{\mathbb{Z}_2}U_{\mathbb{Z}_2}\hat{a}^{(\dagger)}_{p\sigma}U^\dagger_{\mathbb{Z}_2}U_{\mathbb{Z}_2}|\Psi_0\rangle = \Big(\langle\Psi^{N\pm1}_\lambda|U^\dagger_{\mathbb{Z}_2}\Big)\Big[U_{\mathbb{Z}_2}(\bar{X}_{p\sigma} \pm i\bar{Y}_{p\sigma})U^\dagger_{\mathbb{Z}_2}\Big]\Big(U_{\mathbb{Z}_2}|\Psi_0\rangle\Big), \tag{1}$$

$$\langle\Psi^{N}_\lambda|\hat{n}_{p\sigma}|\Psi_0\rangle = \langle\Psi^{N}_\lambda|U^\dagger_{\mathbb{Z}_2}U_{\mathbb{Z}_2}\hat{n}_{p\sigma}U^\dagger_{\mathbb{Z}_2}U_{\mathbb{Z}_2}|\Psi_0\rangle = \Big(\langle\Psi^{N}_\lambda|U^\dagger_{\mathbb{Z}_2}\Big)\Big[U_{\mathbb{Z}_2}(I - \bar{Z}_{p\sigma})U^\dagger_{\mathbb{Z}_2}\Big]\Big(U_{\mathbb{Z}_2}|\Psi_0\rangle\Big), \tag{2}$$

where the transformed bra state, ket state and operator are grouped in brackets at the end of each equation. On the up-spin states, we use the transformation $U_{\mathbb{Z}_2} = \mathrm{CNOT}(3,1)\mathrm{CNOT}(2,0)$; on the down-spin states, we use the transformation $U_{\mathbb{Z}_2} = \mathrm{SWAP}(2,3)\mathrm{CNOT}(3,1)\mathrm{CNOT}(2,0)$, followed by multiplying all the operators by -1; on the spin-balanced states, we use the transformation $U_{\mathbb{Z}_2} = \mathrm{CNOT}(2,3)\mathrm{CNOT}(3,1)\mathrm{CNOT}(2,0)$. After the $\mathbb{Z}_2$ transformation, the first two qubits on the operators and the states are then truncated.

---

* These authors contributed equally to this work
† aminnich@caltech.edu

As an example, consider the transformation of the Pauli string $\bar{X}_{1\uparrow} = ZZXI$. After we apply the transformation CNOT(3, 1)CNOT(2, 0), the operator becomes $-YZYZ$. To truncate qubit 0 and qubit 1, we need to find the constant factor after the transformed Pauli string acts on the first two qubits of the ground state. The constant factor for $\tilde{X}_{1\uparrow}$ is $\langle 01|YZ|11\rangle = i$, where $\langle 01|$ are the bit values on the first two qubits of the transformed up-spin states $\langle \Psi_\lambda^{N\pm1}|U_{\mathbb{Z}_2}^\dagger$ and $|11\rangle$ are the bit values on the first two qubits of the transformed ground state $U_{\mathbb{Z}_2}|\Psi_0\rangle$. The factor of i is then combined with the rest of the Pauli string $-YZ$ to give the final truncated form of the Pauli string $\tilde{X}_{1\uparrow} = -iYZ$. The Pauli strings and qubit state bitstrings before and after the $\mathbb{Z}_2$ symmetry transformations and truncations are given in Table I.

	Pauli string transformation	Original Pauli strings	Transformed Pauli strings	Original qubit state bitstrings	Transformed qubit state bitstrings
Up-spin	$\bar{X}_{0\uparrow} \to \tilde{X}_{0\uparrow}$	$XIII$	II	$(N+1)$-electron:	$(N+1)$-electron:
	$\bar{Y}_{0\uparrow} \to \tilde{Y}_{0\uparrow}$	$iYIII$	ZI	1110, 1011,	10, 11,
	$\bar{X}_{1\uparrow} \to \tilde{X}_{1\uparrow}$	$ZZXI$	$-iYZ$	$(N-1)$-electron:	$(N-1)$-electron:
	$\bar{Y}_{1\uparrow} \to \tilde{Y}_{1\uparrow}$	$iZZYI$	$-XZ$	0100, 0001.	00, 01.
Down-spin	$\bar{X}_{0\downarrow} \to \tilde{X}_{0\downarrow}$	$ZXII$	IZ	$(N+1)$-electron:	$(N+1)$-electron:
	$\bar{Y}_{0\downarrow} \to \tilde{Y}_{0\downarrow}$	$iZYII$	ZZ	1101, 0111.	10, 11.
	$\bar{X}_{1\downarrow} \to \tilde{X}_{1\downarrow}$	$ZZZX$	iYI	$(N-1)$-electron:	$(N-1)$-electron:
	$\bar{Y}_{1\downarrow} \to \tilde{Y}_{1\downarrow}$	$iZZZY$	XI	1000, 0010	00, 01.
Spin-balanced	$Z_{0\uparrow} \to \tilde{Z}_{0\uparrow}$	$ZIII$	$-ZI$	1100,	00,
	$Z_{0\downarrow} \to \tilde{Z}_{0\downarrow}$	$IZII$	$-ZZ$	1001,	01,
	$Z_{1\uparrow} \to \tilde{Z}_{1\uparrow}$	$IIZI$	ZI	0110,	10,
	$Z_{1\downarrow} \to \tilde{Z}_{1\downarrow}$	$IIIZ$	ZZ	0011.	11.

TABLE I: Pauli strings and qubit state bitstrings under $\mathbb{Z}_2$ transformations and truncations. Each Pauli string is characterized as up-spin or down-spin depending on whether it originates from a creation or annihilation operator applied on an up-spin or a down-spin orbital of the ground state, and is characterized as spin-balanced if it originates from a number operator applied on the ground state. The qubit state bitstrings are similarly characterized as up-spin, down-spin or spin-balanced by the type of operator that yields the state after applying on the mean-field ground state $|1100\rangle$, which are consistent with the classification based on the expectation values of the $\mathbb{Z}_2$ symmetry operators $ZIZI$ and $IZIZ$ given in the text.

II. CALCULATION OF TRANSITION AMPLITUDES

In this section, we give the equations used to calculate transition amplitudes in the spectral function and density-density response function from quantities measured on hardware. We use the same notation as in the main text, where $|\Psi_0\rangle$ is the N-electron ground state, $|\Psi_\lambda^{N\pm1}\rangle$ are the $(N\pm1)$-electron states, and $|\Psi_\lambda^N\rangle$ are the N-electron excited states. The transition amplitudes follow the same notation as in Ref. [1], where the transition amplitudes from the ground state to the $(N\pm1)$-electron eigenstates in the calculation of spectral functions are

$$B^{(e)}_{\lambda,p\sigma,q\sigma'} = \langle\Psi_0|\hat{a}_{p\sigma}|\Psi_\lambda^{N+1}\rangle\langle\Psi_\lambda^{N+1}|\hat{a}^\dagger_{q\sigma'}|\Psi_0\rangle, \tag{3}$$

$$B^{(h)}_{\lambda,p\sigma,q\sigma'} = \langle\Psi_0|\hat{a}^\dagger_{p\sigma}|\Psi_\lambda^{N-1}\rangle\langle\Psi_\lambda^{N-1}|\hat{a}_{q\sigma'}|\Psi_0\rangle. \tag{4}$$

The spectral function only requires the diagonal transition amplitudes. Theoretically the (unnormalized) states after restraining the ancilla to $|0\rangle$ or $|1\rangle$ is $\frac{1}{2}(\tilde{X}_{p\sigma} \pm i\tilde{Y}_{p\sigma})\,|\Psi_0\rangle$. Let the tomographed density matrices corresponding to these states be $\rho^\pm_{p\sigma}$. The diagonal transition amplitudes are calculated as the overlap between the $(N\pm1)$-electron eigenstates $|\Psi_\lambda^{N\pm1}\rangle$ and the tomographed density matrices $\rho^\pm_{p\sigma}$:

$$B^{(e)}_{\lambda,p\sigma,p\sigma} = \langle\Psi_\lambda^{N+1}|\rho^-_{p\sigma}|\Psi_\lambda^{N+1}\rangle, \tag{5}$$

$$B^{(h)}_{\lambda,p\sigma,p\sigma} = \langle\Psi_\lambda^{N-1}|\rho^+_{p\sigma}|\Psi_\lambda^{N-1}\rangle \tag{6}$$

Similarly, in the calculation of density-density response functions, we follow the notation in Ref. [2] and define the transition amplitudes from the ground state to N-electron eigenstates as

$$N_{\lambda,p\sigma,p\sigma} = \langle\Psi_0|\hat{n}_{p\sigma}|\Psi_\lambda^N\rangle\langle\Psi_\lambda^N|\hat{n}_{q\sigma'}|\Psi_0\rangle \tag{7}$$

In the diagonal circuits, theoretically the (unnormalized) state after restraining the ancilla qubit to $|1\rangle$ is $\frac{1}{2}(I - \tilde{Z}_{p\sigma})\,|\Psi_0\rangle$. Let the corresponding tomographed density matrix obtained from experiments be $\rho^-_{p\sigma}$. The diagonal transition amplitudes are calculated by taking the overlap of the N-electron eigenstates $|\Psi_\lambda^N\rangle$ and the tomographed density matrix $\rho^-_{p\sigma}$:

$$N_{\lambda,p\sigma,p\sigma} = \langle\Psi_\lambda^N|\rho^-_{p\sigma}|\Psi_\lambda^N\rangle \tag{8}$$

In the off-diagonal circuits, theoretically the (unnormalized) states after restraining the ancilla qubits to $ket10$ or $|11\rangle$ are $\frac{1}{4}[(I - \tilde{Z}_{p\sigma}) \pm (I - \tilde{Z}_{q\sigma'})]\,|\Psi_0\rangle$. Let the corresponding tomographed states obtained from experiments be $\rho^\pm_{p\sigma,q\sigma'}$. The intermediate transition amplitudes obtained directly from $\left|\Psi_\lambda^N\right\rangle$ are defined as

$$T^\pm_{\lambda,p\sigma,q\sigma'} = \langle\Psi_\lambda^N|\rho^\pm_{p\sigma,q\sigma'}|\Psi_\lambda^N\rangle, \tag{9}$$

from which the off-diagonal transition amplitude is determined by Eq. 25 in Ref. [2] (or equivalently Eq. 18 in Ref. [1]) as

$$N_{\lambda,p\sigma,q\sigma'} = e^{-i\pi/4}(T^+_{\lambda,p\sigma,q\sigma'} - T^-_{\lambda,p\sigma,q\sigma'}) + e^{i\pi/4}(T^+_{\lambda,q\sigma',p\sigma} - T^-_{\lambda,q\sigma',p\sigma}). \tag{10}$$

The transition amplitudes $B^{(e)}_\lambda, B^{(h)}_\lambda$ calculated from Eqs. 5 and 6 or N_λ calculated from Eqs. 8 and 10 are then combined with the ground-state energy E_0 as well as the excited-state energies $E^{N\pm1}_\lambda$ or E^N_λ to construct the spectral functions or density-density response functions.

III. CALIBRATION OF THE ITOFFOLI GATE

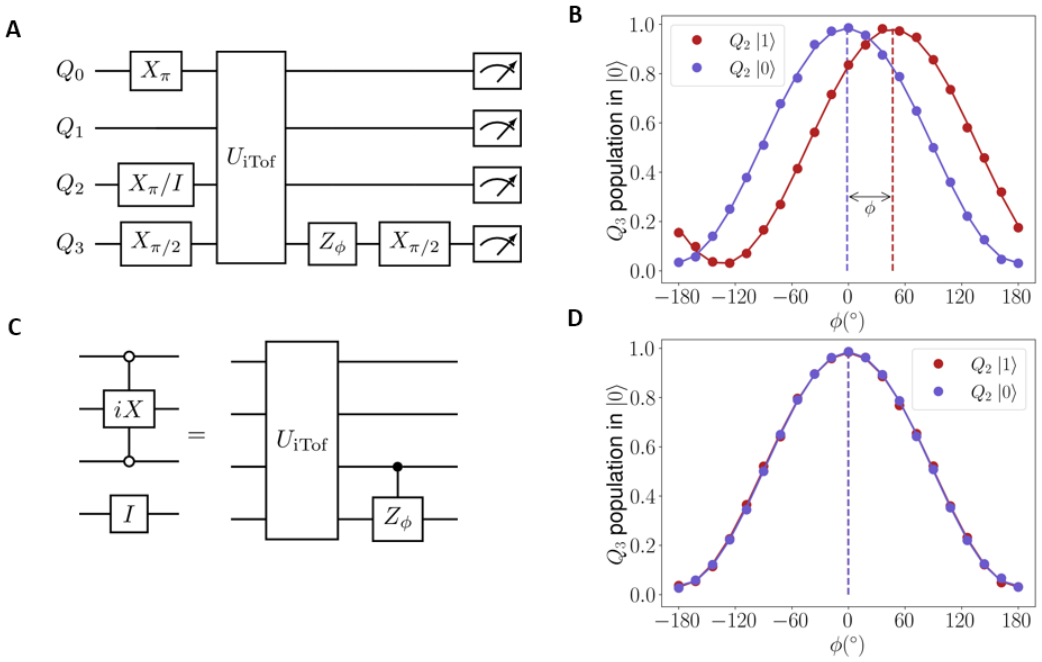

FIG. S1: **Cancellation of spectator error during iToffoli gate.** (**A**) Ramsey protocol for detecting spurious ZZ error between Q_2 and spectator Q_3 during the application of the iToffoli gate. (**B**) $|0\rangle$ population for Q_3 after application of the Ramsey sequence in (A) conditional on the state of Q_2. The relative phase shift between the sinusoidal curves gives the unwanted conditional phase ϕ, which must be corrected. (**C**) A pure iToffoli gate on Q_0-Q_2 is achieved by applying the iToffoli drive from Ref. [3] followed by a CZ_ϕ gate. (**D**) Same as (B) except now the CZ_ϕ correction gate is applied immediately after the iToffoli drive, correcting the unwanted ZZ error.

This work employs the recently developed C-iX-C iToffoli gate [3]. In this section we outline the procedure for eliminating spectator errors during the gate application. Since the gate acts on a three-qubit subset of the full four-qubit subsystem we need to understand and correct the spectator error on the fourth qubit. For concreteness we label qubits Q_i for $i = 0, \ldots, 3$ where the iToffoli gate acts on Q_0, Q_1 and Q_2 with Q_3 as the spectator qubit. States on the four qubits are denoted in the form $|Q_0Q_1Q_2Q_3\rangle$. We run a simple circuit that prepares the system in either $|100+\rangle$ or $|101+\rangle$ (where $|+\rangle = (|0\rangle + |1\rangle)/\sqrt{2}$) and apply the iToffoli gate in a Ramsey-like sequence to determine the Z rotation on Q_3 conditional on the state of its nearest neighbor Q_2 (see Fig. S1a for circuit diagram). We observe an unwanted conditional phase interaction between Q_2 and Q_3 with a conditional phase $\phi = 48.4^\circ$ (see Fig. S1b). This interaction results from the conditional Stark shift between Q_2 and Q_3 when a strong off-resonant drive is applied to Q_2 at the frequency of Q_1 to implement the iToffoli gate [4]. We can use the same effect to undo the conditional phase by applying simultaneous off-resonant drives to Q_2 and Q_3 for a period of 121 ns following the iToffoli drive sequence, which explains why the iToffoli gate duration in our work is longer than that in Ref. [3]. The full pulse sequence and characterization of the residual conditional rotation with the cancellation applied are shown in Figs. S1c and S1d. We benchmark the resulting gate implementation using cycle benchmarking [5]. With this correction, we measure a gate fidelity of 97.8% when isolated to the cycle that only involve qubits Q_0, Q_1 and Q_2, and a small reduction to 96.6% when including the idling spectator qubit Q_3.

Two-qubit CZ and CS/CS† gates are calibrated according to Ref. [4]. Gate fidelities and durations are listed in Table II. Qubit coherence times are listed in Table III for completeness.

Gate	Qubit(s)	Fidelity	Duration (ns)
1Q Cliffords	Q_0	0.9959	60
	Q_1	0.9949	
	Q_2	0.9956	
	Q_3	0.9973	
CZ	(Q_0, Q_1)	0.983	201
	(Q_1, Q_2)	0.987	
	(Q_2, Q_3)	0.980	
CS	(Q_1, Q_2)	0.982	151
iToffoli	(Q_0, Q_1, Q_2)	0.966	413

TABLE II: **Gate fidelities and durations.** Single-qubit Clifford gate fidelities are measured using simultaneous randomized benchmarking [6]. Arbitrary single-qubit gates are decomposed into two real $X_{\pi/2}$ gates (duration 30 ns) and three virtual Z_ϕ gates (duration 0 ns) according to the $ZXZXZ$ decomposition. Two-qubit CZ and CS and three-qubit iToffoli gate fidelities are measured using cycle benchmarking (CB) [5]. All CB fidelities are cycle fidelities including spectator errors on idling qubits.

	Q_0	Q_1	Q_2	Q_3
T_1 (μs)	66	58	65	59
T_{2r} (μs)	38	24	39	47
T_{2e} (μs)	71	77	86	61

TABLE III: **Qubit coherence times.** T_1 (energy decay time), T_{2r} (Ramsey dephasing time) and T_{2e} (spin echo dephasing time) for the qubits used in this work as reported in Ref. [7].

IV. RANDOMIZED COMPILING FOR NON-CLIFFORD GATES

In this section we outline a modified version of randomized compiling (RC) [7, 8] that is applied to the circuits used to compute the observables in the main text. RC is expected to mitigate errors and improve algorithm performance. A broad native entangling gate set is used, consisting of both Clifford gates (CZ) and non-Clifford gates (CS, $\mathrm{CS}^\dagger$, iToffoli). RC is typically used with hard cycles of n-qubit Cliffords where the twirling group $\mathcal{T}$ is chosen to be the group of tensor products of n single-qubit Paulis. By the definition of Clifford gates, for any Clifford C and twirling gate $T \in \mathcal{T}$ there is some $T^c \in \mathcal{T}$ such that $C = TCT^c$. When RC is applied to the hard cycle C_k consisting of Clifford gates, it proceeds by choosing some T_k and T_k^c such that $C_k \to T_k C_k T_k^c$. The single-qubit Paulis T_k and T_k^c are compiled into the easy cycles of single-qubit gates before and after the Clifford cycle C_k, thus keeping the total circuit depth unchanged.

In order to generalize the method to the non-Clifford gates employed in this work we first find the subsets $\mathcal{T}_X \subset \mathcal{T}$ for $X = \mathrm{CS}, \mathrm{CS}^\dagger, \mathrm{iToffoli}$ where for all $T \in \mathcal{T}_X$ there is some $T^c \in \mathcal{T}_X$ such that $X = TXT^c$. RC proceeds in the same way as above except that the twirling gates for hard cycles consisting of gate X are simply chosen from the subset $\mathcal{T}_X$ of Pauli strings that stabilize gate X. Both the CS and $\mathrm{CS}^\dagger$ are stabilized by 4 of the possible 16 two-qubit Pauli strings and the iToffoli is stabilized by 8 of the possible 64 three-qubit Pauli strings. For all these non-Clifford gates the twirling and inversion gates are the same, $T = T^c$. Results "with RC" in the main text involve averaging the experimental bitstring output distributions over 100 equivalent circuit randomizations generated according to the process outlined here, with each circuit measured for 500 shots. These are compared to results "without RC" in which the bare circuit is measured for 50000 shots such that the total number of shots is maintained between the two implementations.

All error processes can be described by a superoperator acting on the density matrix of the full qubit register. Written in the n-qubit Pauli basis this error process matrix is referred to as a Pauli transfer matrix (PTM) with diagonal elements giving Pauli fidelities and off-diagonal elements characterizing the unitary (coherent) and non-unitary (incoherent) errors. As discussed in Refs. [7, 8], applying RC tailors coherent errors into stochastic Pauli noise, which suppresses the off-diagonal elements of the PTM resulting from coherent errors. This holds for the PTM describing errors during the CZ cycles, since these undergo perfect Pauli twirling (in the limit of infinite randomizations). However, in the case of the non-Clifford gate cycles, the twirling is imperfect (since we only twirl over a subset of the n-qubit Pauli strings). As a result, some, but not all, of the off-diagonal elements in the corresponding PTMs are suppressed. In other words, not all coherent errors are tailored to stochastic Pauli noise. This imperfect noise tailoring is the main limitation of our approach to generalizing RC to non-Clifford gates.

We observe a small improvement in the state fidelities when using RC without purification but a much larger improvement when using RC with purification. The improvement in the state fidelities can be explained by the suppression of off-diagonal components of the PTM due to coherent errors, which lowers the overall error rate slightly. As discussed in the main text, if the stochastic Pauli error rates are similar after noise tailoring then the errors are approximately depolarizing and can be largely corrected by McWeeny purification. The deviation of the noise from purely depolarizing is responsible (along with the finite number of randomizations) for the remaining infidelity after RC and purification are applied. Conversely, without RC a larger fraction of the error is a coherent over/under-rotation of the two-qubit Bloch vector which cannot be corrected by purification.

V. ADDITIONAL DATA FOR KH

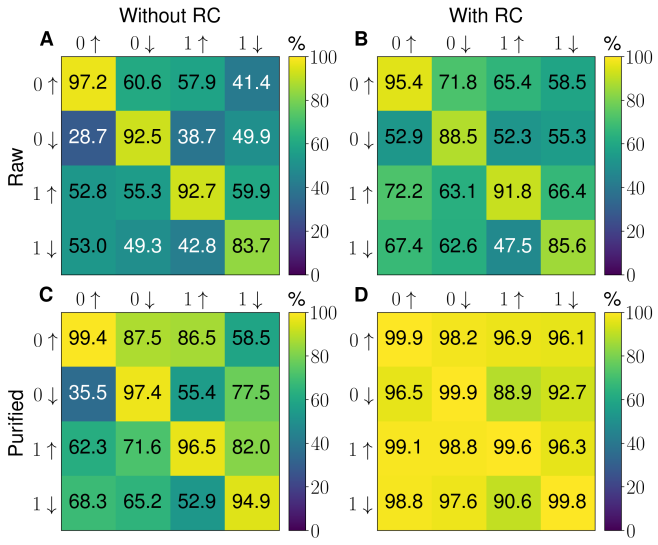

FIG. S2: **System-qubit state fidelities for the response function calculation of KH.** (**A** to **B**) Fidelities between the raw experimental and exact system-qubit density matrices without (A) and with RC (B). (**C** to **D**) Fidelities between the purified experimental and exact system-qubit density matrices without (C) and with RC (D). Layout of the tiles in each panel is the same as in Fig. 5 in the main text. Similar to NaH, without RC, purification raises the average off-diagonal fidelity from 49.2% to 66.9%, but with both RC and purification the average off-diagonal fidelity increases to 95.9%.

This section presents the system-qubit state fidelities and density-density response functions of the KH molecule. Figure S2 shows the system-qubit state fidelities in the response function calculations of KH. In the case of RC without purification, the average off-diagonal fidelity improves from 49.2% in Fig. S2a to 61.3% in Fig. S2b, whereas the average diagonal fidelity slightly decreases from 91.5% in Fig. S2a to 90.5% in Fig. S2b. Purification without RC shows a unified improvement across both diagonal and off-diagonal fidelities, which change to 97.1% and 66.9% from 91.5% and 49.2% respectively when comparing Fig. S2c to Fig. S2a. The most significant improvement again comes from applying both purification and RC, with the average diagonal fidelity 99.8% and average off-diagonal fidelity 95.9% in Fig. S2d.

Figure S3 shows the density-density response functions of KH with all data postprocessed with McWeeny purification. Similar to the case of NaH, the iToffoli decomposition exhibits a better agreement with exact results in the absence of RC. For χ_{00} without RC in Fig. S3a, the deviations from exact peak heights are 1.0% and 13.9% for the iToffoli decomposition, but are 41.6% and 17.1% for the CZ decomposition. For χ_{01} without RC in Fig. S3c, although both decompositions fail to capture the peak at 24 eV, the iToffoli decomposition reproduces the exact peak with an 8.2% deviation while the CZ decomposition results in only around half of the peak height for the peak at 1.4 eV. When RC is used to construct the circuits, the results are comparable between the two decompositions. For χ_{00} with RC in Fig. S3b, the peak height deviations in the two peaks are 17.0% and 10.7% for the iToffoli decomposition, which are slightly better than the CZ decomposition results of 21.6% and 20.8%. For χ_{01} with RC in Fig. S3d, the CZ decomposition exhibits a better agreement, with peak height deviations of 4.2% and 7.7%, compared to the values from the iToffoli decomposition of 26.6% and 45.5%.

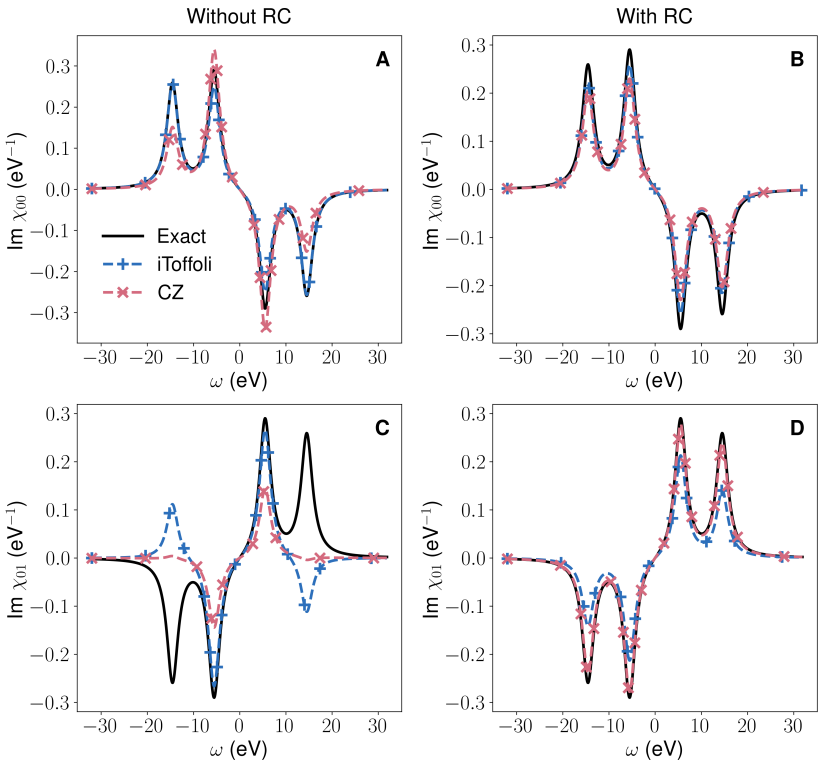

FIG. S3: **Density-density response function of KH**. (A) Im χ_{00} without RC. (B) Im χ_{00} with RC. (C) Im χ_{01} without RC. (D) Im χ_{01} with RC. All experimental results are postprocessed with McWeeny purification on the system-qubit states after constraining to the ancilla bitstring subspace. A broadening factor of $\eta = 1.5$ eV is used to produce the spectra. Similar to NaH, the iToffoli decomposition yields qualitatively better results compared to the CZ decomposition in the absence of RC. After RC is applied, results from the two decompositions are comparable.

[1] T. Kosugi and Y.-i. Matsushita, Construction of Green's functions on a quantum computer: Quasiparticle spectra of molecules, Phys. Rev. A **101**, 012330 (2020).

[2] T. Kosugi and Y.-i. Matsushita, Linear-response functions of molecules on a quantum computer: Charge and spin responses and optical absorption, Phys. Rev. Res. **2**, 033043 (2020).

[3] Y. Kim, A. Morvan, L. B. Nguyen, R. K. Naik, C. Jünger, L. Chen, J. M. Kreikebaum, D. I. Santiago, and I. Siddiqi, High-fidelity three-qubit iToffoli gate for fixed-frequency superconducting qubits, Nat. Phys. **18**, 783 (2022).

[4] B. K. Mitchell, R. K. Naik, A. Morvan, A. Hashim, J. M. Kreikebaum, B. Marinelli, W. Lavrijsen, K. Nowrouzi, D. I. Santiago, and I. Siddiqi, Hardware-efficient microwave-activated tunable coupling between superconducting qubits, Phys. Rev. Lett. **127**, 200502 (2021).

[5] A. Erhard, J. J. Wallman, L. Postler, M. Meth, R. Stricker, E. A. Martinez, P. Schindler, T. Monz, J. Emerson, and R. Blatt, Characterizing large-scale quantum computers via cycle benchmarking, Nature Comms. **10**, 5347 (2019).

[6] J. M. Gambetta, A. D. Córcoles, S. T. Merkel, B. R. Johnson, J. A. Smolin, J. M. Chow, C. A. Ryan, C. Rigetti, S. Poletto, T. A. Ohki, M. B. Ketchen, and M. Steffen, Characterization of addressability by simultaneous randomized benchmarking, Phys. Rev. Lett. **109**, 240504 (2012).

[7] A. Hashim, R. K. Naik, A. Morvan, J.-L. Ville, B. Mitchell, J. M. Kreikebaum, M. Davis, E. Smith, C. Iancu, K. P. O'Brien, I. Hincks, J. J. Wallman, J. Emerson, and I. Siddiqi, Randomized Compiling for Scalable Quantum Computing on a Noisy Superconducting Quantum Processor, Phys. Rev. X **11**, 041039 (2021).

[8] J. J. Wallman and J. Emerson, Noise tailoring for scalable quantum computation via randomized compiling, Phys. Rev. A **94**, 052325 (2016).